

3D imaging and mechanical modeling of helical buckling in *Medicago truncatula* plant roots

Jesse L. Silverberg^{a,1}, Roslyn D. Noar^{b,2}, Michael S. Packer^a, Maria J. Harrison^b, Christopher L. Henley^a, Itai Cohen^a, and Sharon J. Gerbode^{a,3}

^aDepartment of Physics, Cornell University, Ithaca, NY 14853; and ^bBoyce Thompson Institute for Plant Research, Cornell University, Ithaca, NY 14853

Edited by William R. Schowalter, Princeton University, Princeton, NJ, and approved September 5, 2012 (received for review June 4, 2012)

We study the primary root growth of wild-type *Medicago truncatula* plants in heterogeneous environments using 3D time-lapse imaging. The growth medium is a transparent hydrogel consisting of a stiff lower layer and a compliant upper layer. We find that the roots deform into a helical shape just above the gel layer interface before penetrating into the lower layer. This geometry is interpreted as a combination of growth-induced mechanical buckling modulated by the growth medium and a simultaneous twisting near the root tip. We study the helical morphology as the modulus of the upper gel layer is varied and demonstrate that the size of the deformation varies with gel stiffness as expected by a mathematical model based on the theory of buckled rods. Moreover, we show that plant-to-plant variations can be accounted for by biomechanically plausible values of the model parameters.

morphogenesis | plant biomechanics | biological chirality | root growth and remodeling

Plant growth and crop productivity depend on the ability of plant root systems to secure water and nutrients from the heterogeneous terrestrial environment in which they grow. Soil compaction resulting from agricultural activities or from environmental changes such as drought impedes root growth and consequently has severe negative effects on yield (1). As world population continues to rise, plant breeding programs are challenged with the need to increase crop yields while facing a decline in agricultural soil quality including increased mechanical impedance of soil. Thus, there is a need to better understand the strategies that roots employ to grow in mechanically heterogeneous environments. Pioneering investigations have described the buckling of roots traversing air gaps in soils (2–4) and measured the forces generated during root growth (5–8); however, further progress has been hindered by the opaque nature of soil.

Here, we build on recent imaging techniques (9–14) to investigate the growth of roots through mechanically heterogeneous environments. Our apparatus is distinct in that it employs a laser sheet and a translational stage to rapidly scan the region of root growth. Using this three-dimensional (3D) time-lapse imaging system, we observe primary *Medicago truncatula* roots growing through a transparent hydrogel composed of a compliant upper layer and stiff lower layer. The structural heterogeneity in the growth medium allows us to mechanically perturb the root in a controlled fashion. Consistently, we find the roots deform into a helical shape before penetrating into the lower layer as shown in Fig. 1. Because the length of the helical region is comparable to the length of the elongation zone in *Medicago* plants, it may be supposed that this morphology is purely a biological process such as circumnutation. However, our analysis reveals that (i) when the root encounters the stiff lower layer, tissue near the root tip twists via a remodeling process, and (ii) the mechanical buckling of the twisted root within the gel accounts for the observed helical shape. Collectively, these results demonstrate an important example of the interplay between mechanics and morphology during root growth in heterogeneous environments.

Experimental Procedures

Helical Root Growth. A two-layer medium 8 cm thick was prepared using a transparent isotropic nutrient gel (15) solidified with two different concentrations of Gelrite. Using an Anton Paar rheometer, we measured the shear modulus and found $G_B \approx 1,500$ Pa for the bottom layer and $G \approx 400$ Pa for the top layer (see *SI Text*). Thus, the abrupt increase in stiffness at the gel/gel interface forms an elastic mechanical barrier to root growth. Through most of the top layer, roots grew straight down; if present, any root circumnutation was too subtle to observe. Just above the interface, however, we observed pronounced helical root deformations as shown in Fig. 1. Repeating the experiment, we found the general root morphology was reproducible, though each time there were variations in the shape and size of the helical deformations. From our visual inspections, we also noted that 74% of the root helices were right-handed, whereas the remaining 26% were left-handed (estimated uncertainty $\pm 9\%$).

Mechanical Interpretation. Based on our observations, we interpret the helical deformation as a form of mechanical buckling that occurs when the tip's motion is halted by the stiff gel while the root continues to elongate. To investigate how this driving mechanism can lead to the observed root shapes, we developed a simple experimental model consisting of an axially compressed metal rod as a mechanical analog for the root. The rod, a nylon-coated stainless steel wire 0.4 mm in diameter and 8 cm long, was held vertically with the top end fixed to a stationary plate using epoxy. Axial force was manually applied with tweezers by pushing the lower end upward to compress the filament. When the wire is compressed in air, the resulting long wavelength deformation shown in Fig. 2A is consistent with the expected Euler buckling; the deformation occurs in a plane (Fig. 2A, *Inset*) and extends the full length of the wire.

In contrast, the root deformations were localized close to the tip (Fig. 1). To produce this effect in the mechanical model, we embedded the same wire in gelatin (Jell-O) and again applied axial compression from the lower end leading to reversible deformations. As shown in Fig. 2B and *Inset*, localized planar buckling was induced near the region where force was applied. This can be understood in the following manner. Buckling takes a sinusoidal form if the longitudinal stress is uniform throughout (16). However, the wire surface and gel adhere without slip so that displacements of the wire lead to shear deformations of the gel. Force

Author contributions: J.L.S., M.J.H., C.L.H., I.C., and S.J.G. designed research; J.L.S., R.D.N., M.S.P., and S.J.G. performed research; J.L.S., C.L.H., I.C., and S.J.G. analyzed data; and J.L.S., M.J.H., C.L.H., I.C., and S.J.G. wrote the paper.

The authors declare no conflict of interest.

This article is a PNAS Direct Submission.

¹To whom correspondence should be addressed. E-mail: JLS533@cornell.edu.

²Present address: Department of Plant Pathology, North Carolina State University, 2510 Thomas Hall, Raleigh, NC 27695-7616.

³Present address: Department of Physics, Harvey Mudd College, 301 Platt Blvd., Claremont, CA 91711-5990.

This article contains supporting information online at www.pnas.org/lookup/suppl/doi:10.1073/pnas.1209287109/-DCSupplemental.

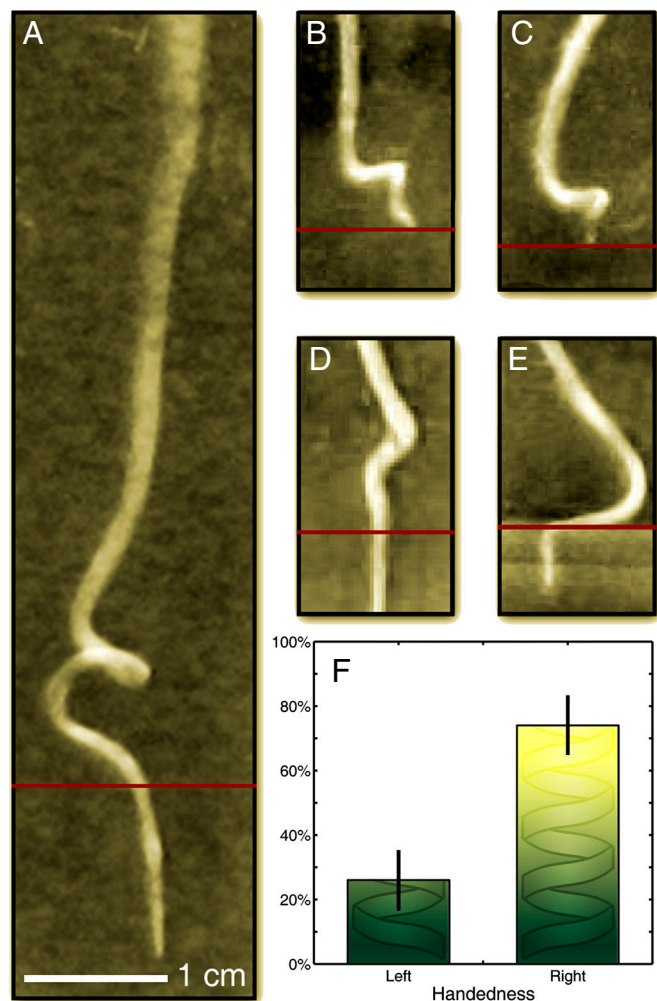


Fig. 1. (A–E) This gallery of contrast-enhanced digital photographs is a representative selection of the helical root growth observed at the interface of compliant (above red line) and stiff (below red line) gels. They illustrate both the consistency and variation of the phenomenon. (F) The number of left- and right-handed helices were asymmetrical as shown by the histogram (estimated uncertainty $1/\sqrt{N}$).

balance shows that this gel shearing force accumulates along the wire's length, reducing the wire's internal longitudinal stress and attenuating the applied force. Thus, localized buckling occurs when a finite portion of the wire is above the buckling threshold while the rest is below (17). In order to produce a 3D helical shape, we added one additional feature: We manually twisted one end of the wire during compression. As Fig. 2C and *Inset* show, this combination of compression and twisting within a supporting medium produced a localized helical deformation like the shape observed in roots.

To check whether a similar twisting mechanism is at play during helical root growth, we fluorescently stained the epidermis of roots with a solution containing 10 $\mu\text{g}/\text{mL}$ of 5-(4,6-dichlorotriazinyl)aminofluorescein and imaged them with a confocal microscope. For roots grown in unlayered gels, cell files were aligned vertically in columns along the entire length of the root (Fig. 3A and *Inset*). In layered gels where the roots encountered the stiff lower layer, cell files were twisted around the axis of the root in the helical region (Fig. 3B), and untwisted everywhere else. The localization of twisting shows that unobstructed root growth generally occurs without a visible preexisting chirality. Moreover, we extracted and compressed several straight roots, observing planar nonlocalized buckling in all cases, ruling out internal helicity as a twisting mechanism. Additionally, the distribution of handedness

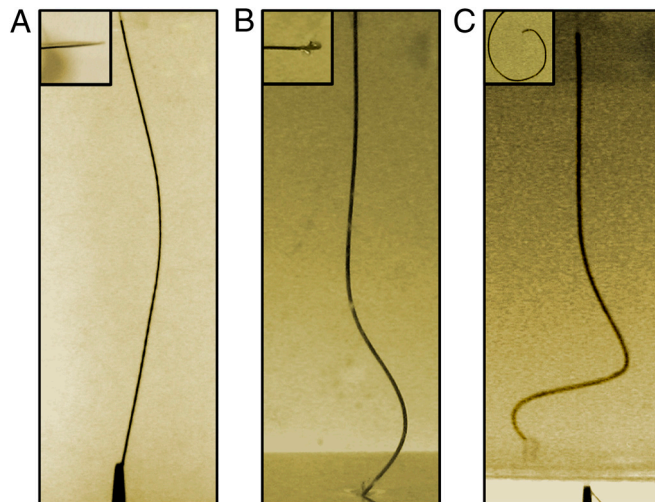


Fig. 2. As a mechanical analog to root buckling, we axially compressed a metal filament from the lower end. In all images, the top end is epoxied to a plate (clamped boundary condition), while the lower end is held with tweezers (hinged boundary condition). (A) Euler buckling is observed when the filament is suspended in air. (B) Embedding the filament in a gel yields dampened short wavelength oscillations. (C) Twisting the lower end of the gel-embedded filament while applying compression yields a helical shape similar to the roots. All *insets* are top-down views and show whether the buckling was planar or 3D.

for the root morphology shown in Fig. 1F demonstrates that passive physical instabilities such as those seen during the coiling of poured viscous liquids (18) are insufficient for generating root twisting because they would lead to, on average, equal numbers of either handedness. Finally, we note that differential elongation as currently understood would only produce planar buckling.

Collectively, these observations suggest that the twisting involved in helical buckling arises from a touch-activated biological remodeling in response to axial loads. Though the microscopic dynamics were not observable in our experiments, the process

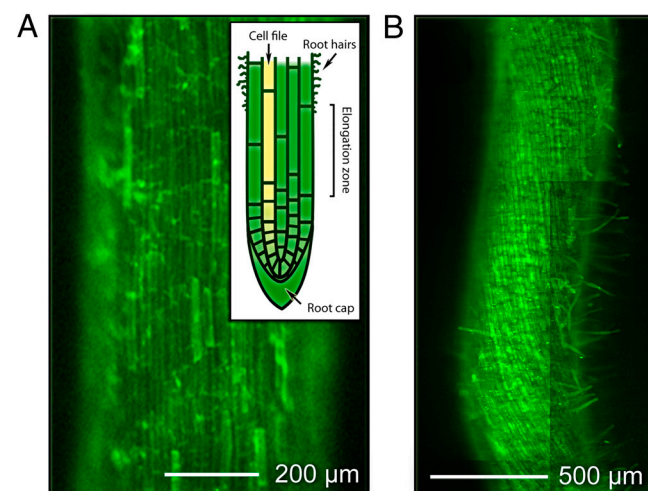


Fig. 3. Roots were stained and imaged with confocal microscopy to examine the local surface structure. The *inset* illustrates schematically the developmental physiology of the growth zone in roots. In particular, cells are arranged in vertical columns called cell files, which extend from the root cap toward the soil surface. Primary root growth occurs when the cells near the root cap undergo cell division and elongation, adding material within each column. Consequently, the cell file pattern serves as an indicator for the history of root growth. (A) A section of a straight, undeformed root exhibits vertical cell files. (B) In contrast, cell files within the helically deformed region are wrapped around the root's axis, indicating a twisting of the root.

may be related to the thigmotropic-modulated gravitropism previously reported in *Arabidopsis* (19).

Model

The wire model provides a qualitative understanding of helical root buckling. It is unclear, however, whether the mechanistic interpretation of the root as a twisted buckled rod embedded in a gel can capture the plant-to-plant variations typically seen in our experiments (Fig. 1). Toward this end, we (*i*) developed an experimental protocol for measuring variations in root morphology, (*ii*) developed a mathematical formulation of the buckled rod model, (*iii*) fitted the model to the data, and (*iv*) determined whether the fitted values of the model parameters are biomechanically plausible.

Measurements of Root Geometry. To quantify the plant-to-plant variations in root morphology, we measured the shape of the helical regions using a unique imaging technique we developed for 3D time-lapse imaging of growing roots (3D-TIGR). In essence, our apparatus (Fig. 4) scans the region of root growth with a laser sheet while taking image slices spaced every 0.150 mm. Each scan took less than 5 min. The image slices were then processed in IMARIS 6.0 to create a 3D reconstruction of the root and to extract its spatial coordinates $\langle x(z), y(z), z \rangle$.

The total imaging time for each root growth experiment was approximately 100 h. To establish an experimental protocol for measurement of the helical morphology, we recorded time-lapse movies for 13 roots at a rate of one 3D scan per hour (Movies S1–S3). These movies reveal that when steady growth is impeded by the stiff gel, the root abruptly deforms in the transverse direction as expected for a buckled rod. Moreover, because the shape is already helical, root twisting must initiate before buckling. Continued growth leads to the stereotypical shapes shown in Fig. 1. After the tip penetrates into the lower layer, the radial extent of the helix rapidly shrinks by $30 \pm 10\%$ (Fig. S1). Thus, for the following analysis, we scanned each root after it passed through the barrier and then linearly scaled the transverse size of the helix by 1.43 to recover the buckled shape before penetration.

To quantify the size of the helical deformation, we defined two length scales, the average vertical extent of the helix ($\langle L \rangle$), and the average squared radius of the helix ($\langle R^2 \rangle$). These longitudinal and transverse measures are depicted schematically in the *insets* of Fig. 5. We calculated $\langle L \rangle$ and $\langle R^2 \rangle$ from the scaled 3D-TIGR root coordinate data using

$$\langle L \rangle = \frac{[\int r^2 dz]^2}{\int r^4 dz}, \quad \langle R^2 \rangle = \frac{\int r^4 dz}{\int r^2 dz}, \quad [1]$$

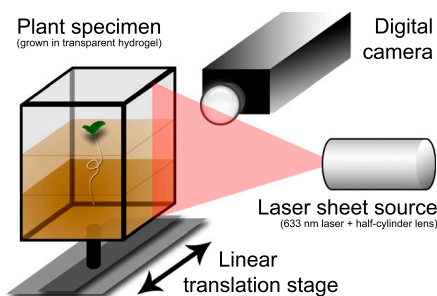


Fig. 4. This schematic illustration highlights the essential features of the 3D-TIGR apparatus used to quantify helical root buckling. An automated data acquisition program translates the plant specimen through a laser sheet, while a digital camera captures a series of images of reflected light. Because the growth medium is transparent, only light scattered off the root is recorded in the scan.

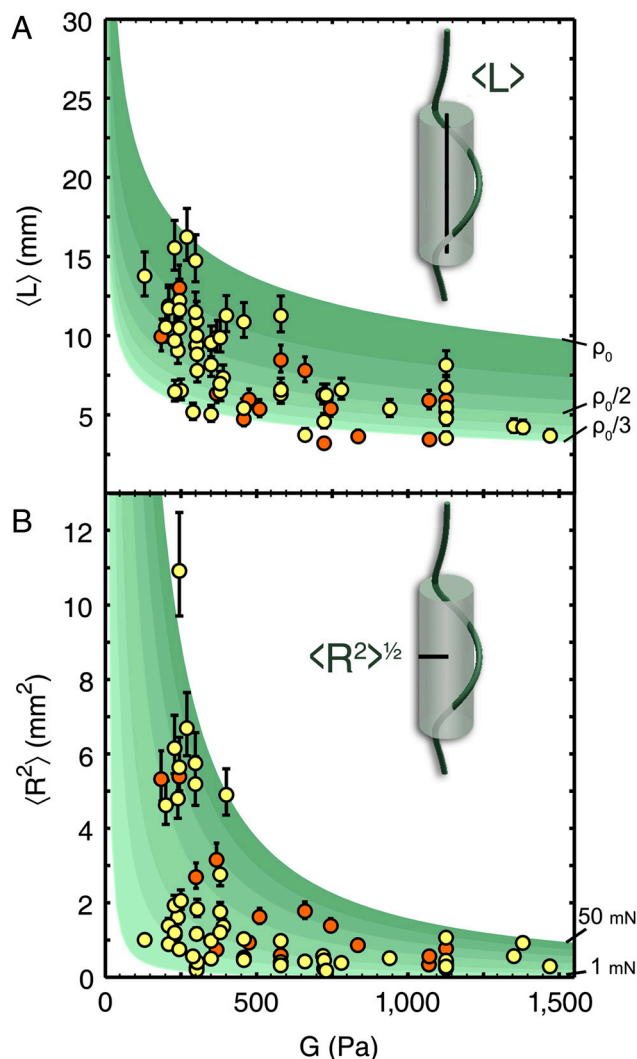


Fig. 5. Experimental measurements of the (A) longitudinal and (B) transverse length scales of the helical root morphology as defined in Eq. 1 are plotted against the top gel layer modulus G . We find that both length scales decrease in stiffer gels, whereas their variations at a given stiffness tend to increase in compliant gels. The contours were produced by numerical integration of the equations in Eq. 2 over a range of parameter values given by the contours shown in Fig. 6. In particular, the spread in $\langle L \rangle$ was found to correlate with variations in the bending modulus (Fig. 6B, green contours), whereas the spread in $\langle R^2 \rangle$ was found to correlate with variations in the tip compressive force (Fig. 6D, green contours). Red data points are roots that violated the small deflection approximation used in the mathematical model.

where $r^2 = x(z)^2 + y(z)^2$ is measured from the central axis of the helix, which was oriented to coincide with the z axis. Bounds of the integrals were defined by noting the curvature of $r(z)$ is zero outside the helical region; however, we note the equations in Eq. 1 are generally insensitive to the choice of endpoints.

For the gel system shown in Fig. 1 where $G \approx 400$ Pa, there were substantial root-to-root variations in both $\langle L \rangle$ and $\langle R^2 \rangle$ (Fig. 5). To gain further insight into the range of possible root morphologies and their dependence on G , we grew 67 plants in gels where the top layer modulus was varied from about 100 to 1,500 Pa. For these gels, we saw no apparent dependence of the root radius or length on the modulus; however, $\langle L \rangle$ and $\langle R^2 \rangle$ were found to depend inversely on G (Fig. 5). Furthermore, the spreads in $\langle L \rangle$ and $\langle R^2 \rangle$ at fixed G are also inversely related to the modulus: At $G \approx 250$ Pa there is a three-fold variation in $\langle L \rangle$ and over an order of magnitude variation in $\langle R^2 \rangle$, whereas at $G \approx 1,500$ Pa these variations are significantly reduced.

Evidently, the root geometry and its variations are strongly dependent on the stiffness of the growth medium.

Theoretical Model: Development and Quantitative Fitting. For simplicity, we modeled the root tissue from the helical region as a homogeneous inextensible isotropic cylindrical rod. These assumptions are consistent with experimental observations: (i) Root cells are roughly 10^2 times smaller than the typical dimensions of the helix (Fig. 3), (ii) the time scale for growth is much longer than the buckling instability time scale (Movies S1–S3), and (iii) neither the material properties nor root radius vary significantly over the length of the helical region (20). These assumptions allow the rod to be described by a constant bending modulus EI with Young's modulus E and moment of area I . Next, we embed the theoretical rod in a linear elastic gel with shear modulus G . Based on the growth of fine hairs that anchor the root to its growth medium (8, 20), we assume a no-slip boundary condition. For simplicity, we neglect viscoplastic effects in the gel; rheological measurements, elastic relaxation of roots after penetration into the lower gel, and the absence of cavitation bubbles support this assumption. Finally, we specifically focus on variations in root morphology and therefore exclude the dynamic components of touch-activated twisting from our model.

The general data trends can be understood by basic scaling arguments. A force T_0 greater than the critical buckling force F_c causes a rod to buckle into an arc of length L with amplitude u and bending energy $\sim EI(u/L^2)^2 \times L$. The buckled rod causes a volume $\sim L^3$ of the embedding gel to deform with an energy $\sim G(u/L)^2 \times L^3$. For a fixed force T_0 , we minimize the sum of these energies with respect to arc length to find $L \sim \ell$, where the characteristic length scale $\ell \equiv (EI/G)^{1/4}$. Therefore, we expect $\langle L \rangle \sim G^{-1/4}$. Furthermore, the scaled transverse displacement $\langle R^2 \rangle / \ell^2$ increases with the scaled excess force $(T_0 - F_c) / F_0$, where the characteristic force scale $F_0 \equiv [(EI)G]^{1/2}$. Thus, $\langle R^2 \rangle$ will have an inverse dependence on G due to the factor of ℓ^2 and because F_0 is larger in stiffer gels. These arguments for $\langle L \rangle$ and $\langle R^2 \rangle$ predict smaller root deformations in stiffer gels. Although the experimental measurements qualitatively agree, the data have significant scatter and are too limited in range to test the predicted scaling.

Using a more detailed application of the theoretical rod model, we test whether mechanical buckling can account for the entire morphology of each root as well as the individual variability. Parameterizing the centerline of the rod as $\langle x(z), y(z), z \rangle$, the key mechanical quantities of interest are the longitudinal compressive force $T(z)$ and the axial moment $M_z(z)$. Within the small deflection approximation where the infinitesimal element of arclength $ds \cong dz$, the equations of equilibrium for the transverse forces per unit length are

$$\begin{aligned} EIy'''' - [M_z(z)x']'' - [T(z)y']' &= -\alpha y, \\ EIx'''' + [M_z(z)y']'' - [T(z)x']' &= -\alpha x. \end{aligned} \quad [2]$$

Primes indicate differentiation with respect to z , and $\alpha \approx 2G$ is the effective transverse spring constant per unit length due to the gel elasticity (see SI Text for detailed derivation). In each equation, the left-hand side includes terms for (i) the bending force of the rod, (ii) the force required for torque balance when the centerline is twisting, and (iii) the projection of $T(z)$ along the rod's path. To calculate the dependence of $\langle L \rangle$ and $\langle R^2 \rangle$ on the gel modulus, we first determine $T(z)$, $M_z(z)$, and the appropriate boundary conditions.

We find the compressive force $T(z)$ by considering growth just prior to buckling when the tip has made contact with the stiff lower gel. Because growth is obstructed, root elongation, which occurs at the tip, leads to a uniform longitudinal upward displacement of the entire root. However, fine hairs anchor the root to

the embedding gel, leading to a downward linear restoring force acting on each portion of the root. Assuming no slip between the root and gel, force balance yields

$$T(z) = -T_0(1 - z/Z), \quad [3]$$

where T_0 is the force applied on the root tip by the lower gel and Z is the length of the root. Eq. 3 models the nonuniform compressive force previously discussed.

In roots, the moment $M_z(z)$ arises from the response of individual cells to their local loading conditions and likely results in a remodeling of the root's elastically unstrained reference state. Because the in vivo details are unknown, we take a phenomenological approach and calculate the required moment to produce a given helical morphology by integrating the equations of equilibrium over 20 experimentally measured root contours (see SI Text). Generally, we find the moment is zero outside the helical region, and nonzero within (Fig. S2). Following this trend, we approximate the functional form as

$$M_z(z) = M_0 = \text{constant}. \quad [4]$$

M_0 has two contributions: (i) the previously discussed remodeling of root tissue, and (ii) the root's intrinsic elasticity. Although the latter contribution gives rise to a twist per unit length $\Delta\tau$ beyond the remodeled reference state, both are related to the observed cell file twisting. If elasticity dominates the moment, then $M_0 = C(z)\Delta\tau(z)$, where for a homogeneous isotropic inextensible rod, the torsional rigidity $C(z) = (2/3)EI = \text{constant}$ (21). Thus, the expression $\Delta\tau(z) = 3M_0/2EI = \text{constant}$ is a bound on the rate of cell file twisting.

To determine the boundary conditions and test the model, we performed an iterative nonlinear least-squares fitting of the root coordinate data from the helical region to Eqs. 2–4. Specifically, we use the Levenberg–Marquardt algorithm to determine the best-fit values for the model parameters EI , T_0 , and M_0 , as well as the transverse forces and moments at both ends of the fitting interval. This process was repeated for all roots; 49 of the 67 plants had convergent fits (Fig. 6A). Of the nonconvergent fits, an inspection of the complete 3D-TIGR data revealed helical morphologies that violated the small deflection approximation.

From the convergent fits, we infer the appropriate boundary conditions. Generally, the transverse forces $F_x \propto x$ and $F_y \propto y$ vanished at both ends. Similarly, the transverse moments $M_x \propto x''$, and $M_y \propto y''$ were smallest at $z = 0$, while the tangent components x' and y' vanished at $z = Z$. Collectively, these results yield a hinged boundary condition $(x, y, x'', y'' = 0)$ at the bottom of the rod, and a clamped boundary condition $(x, y, x', y' = 0)$ at the top. Additionally, we found the majority of best-fit values for EI and T_0 were spread over two orders of magnitude (Fig. 6B and D, yellow crosses), while the estimated twist per unit length $3M_0/2EI$ was clustered between 0.1 and 1.0 rad/mm (Fig. 6E, yellow crosses).

Independent Checks of Fitted Parameters. To check whether the values for the fitting parameters are biomechanically plausible, we independently estimated EI , T_0 , and M_0 . Starting with the bending modulus, we measured EI for 16 roots in a three-point bending apparatus (see SI Text). Unfortunately, root tissue from the helical region was too short and fragile to work with. Therefore, we made measurements on the older, more lignified root tissue between the helical growth and the base of the plant. Because this tissue was typically 5–7 days old, it was thicker and easier to work with. Indeed, we measured $EI_M = (3.5 \pm 1.6) \times 10^{-7} \text{ Nm}^2$ (SD) (Fig. 6B, black solid and dashed lines), which agrees with the upper range predicted by fitting.

Concerning root-to-root variations, it is unlikely that Young's modulus E varies enough to account for the spread in the fitted

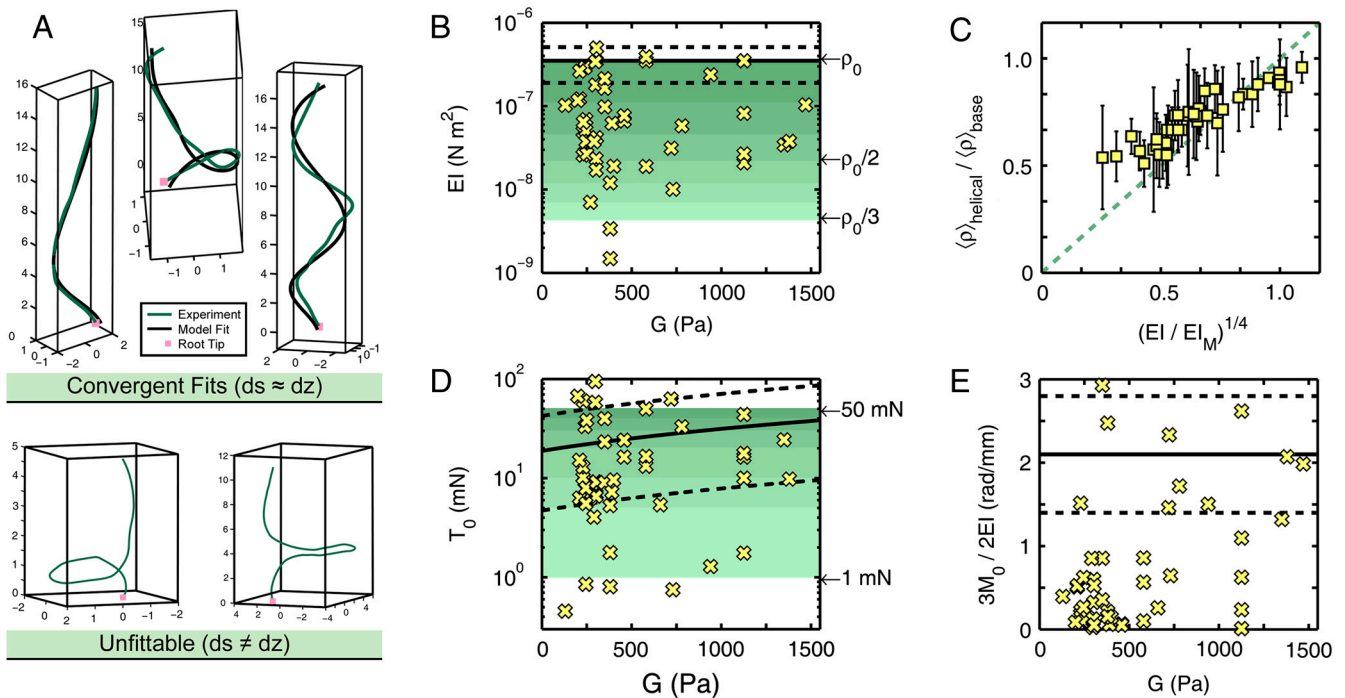


Fig. 6. This figure shows the results of numerical fits of the equations in Eq. 2 to experimental root coordinate data. (A) Examples of best fits that converged ($ds \approx dz$). In each case, the green curve is experimental data, the black curve is the best fit, the red square is the root tip, and the scale is in millimeters. In the lower portion, we show root coordinate data that was unifiable due to violations of the small deflection approximation ($ds \neq dz$). (B) The best-fit values for the bending modulus EI are plotted against G (yellow crosses). The majority of values are spread over two orders of magnitude. Here, ρ_0 is the root radius corresponding to the measured average bending modulus EI_M (solid and dashed black lines). Variations in ρ_0 by up to one-third account for most of the spread in the fitted values of EI . Noting that $\rho/\rho_0 = (EI/EI_M)^{1/4}$ these results can be used to predict the tapering of the root radius. (C) Comparing the predicted reduction in root radius $(EI/EI_M)^{1/4}$ to the measured reduction $\langle \rho \rangle_{\text{helical}} / \langle \rho \rangle_{\text{base}}$, we find a correlation confirming that variations in the root radius account for the variations in EI . (D) The best-fit values for the tip compressive force T_0 are shown as a function of G (yellow crosses). The spread has substantial agreement with estimates based on experimentally observed dimpling of the gel interface (solid and dashed black lines), though various factors can cause T_0 to deviate from these bounds. (E) The best-fit values for the estimated twist per unit length $3M_0/2EI$ are plotted as a function of G . The experimentally measured twist is plotted for comparison (solid and dashed black lines).

EI . However, if each root has a distinct radius ρ in the helical region, there can be significant variation in the moment of area $I = (\pi/4)\rho^4$ (Fig. 6B, green contours). To investigate this possibility, we assumed E was constant and that differences between the fitted EI and measured EI_M were due solely to ρ . We then calculated the predicted reduction in root radius relative to mature tissue, $(EI/EI_M)^{1/4}$. From the raw 3D-TIGR data, we measured the average root radius in the helically buckled and basal regions to find $\langle \rho \rangle_{\text{helical}} / \langle \rho \rangle_{\text{base}}$. Comparing these quantities, we find a strong correlation confirming that variations in the root radius can account for spread in the fitted EI (Fig. 6C).

Although T_0 is difficult to measure experimentally, estimates of its value can be made from deformations in the gel interface induced by the root tip. Detailed calculations (21) show that a point force T_D on a half-infinite elastic medium causes a dimple of depth D and radius ρ . Here, ρ is the same as the root tip radius. Because we have two elastic mediums, $T_D = 4\pi(G + G_B)D\rho$, where G and G_B are the shear moduli of the top and bottom gel layers, respectively. Visual observations show $D \approx 2 \pm 1$ mm, and $\rho \approx 0.50 \pm 0.25$ mm.

Assuming $T_0 \approx T_D$, we estimate the tip force along with upper and lower bounds as a function of the top gel modulus (Fig. 6D, black solid and dashed lines). Values range from 5 to 100 mN and agree with 80% of the fits, consistent with the possibility that some of the scatter in T_0 arises from variations in G . Additional estimates based on a Hertz contact or the gel fracture strength are consistent with these results (see SI Text). Deviations from theoretical expectations can be accounted for by imperfect coupling between the root and the gel or variations in the root tip's angle of attack resulting in a decreased normal force on the gel surface.

To check the range of best-fit values for the moment M_0 , we used confocal images to measure the cell file angle with respect to the root axis in the helically buckled region. Imaging several roots, we found an average twist of $\tau_M = (2.1 \pm 0.7)$ radians/mm (SD) (Fig. 6E, black solid and dashed lines). Comparing with the fits, we see τ_M overestimates $\Delta\tau = 3M_0/2EI$. This overestimate can be attributed to remodeling of the unstrained reference state wherein an elastically relaxed configuration still exhibits twisted cell files. Root-to-root variation in M_0 can be attributed to differences in the growth rate of individual plants.

Collectively, the range of best-fit values for the bending modulus EI , the tip compressive force T_0 , and the moment M_0 are consistent with our independent checks and thus biomechanically plausible. These findings demonstrate our simplified mathematical model is capable of quantitatively accounting for the variations observed in the root morphology.

Relating Model Parameters to Root Morphology. To identify the connection between variation in specific model parameters and root morphology, we used Eqs. 2–4 to simulate the dependence of $\langle L \rangle$ and $\langle R^2 \rangle$ on EI , T_0 , and M_0 . Specifically, we performed sets of numerical solutions while systematically varying the model parameters within the ranges determined by fitting. In our simulation, we increased T_0 until the rod buckled, at which point we evaluated $\langle L \rangle$ and $\langle R^2 \rangle$ from the solution $\langle x(z), y(z), z \rangle$.

Over the experimental range of G , we found that $\langle L \rangle$ depends primarily on EI , $\langle R^2 \rangle$ depends primarily on T_0 , while neither depends strongly on M_0 . Specifically, we fixed $T_0 = 10$ mN, $3M_0/2EI = 0.45$ radians/mm, and varied EI over the range illustrated by the green contours in Fig. 6B, producing a

corresponding set of contours for $\langle L \rangle$ as a function of G (Fig. 5A). Similarly, we fixed $EI = 2.2 \times 10^{-8} \text{ Nm}^2$, $3M_0/2EI = 0.45 \text{ radians/mm}$, and varied T_0 over the range illustrated by the green contours in Fig. 6D. This produced a set of contours for $\langle R^2 \rangle$ as a function of G (Fig. 5B). The dependence of $\langle R^2 \rangle$ on EI and $\langle L \rangle$ on T_0 was negligible and could not account for variations at fixed G . Finally, we fixed $EI = 2.2 \times 10^{-8} \text{ Nm}^2$, $T_0 = 10 \text{ mN}$, and varied $3M_0/2EI$ from 0.1 to 0.7 radians/mm to produce a set of contours (Fig. S3) that showed weak sensitivity of $\langle L \rangle$ and $\langle R^2 \rangle$ on M_0 .

From the contours in Fig. 5, we are able to read off the scaling relations for $\langle L \rangle$ and $\langle R^2 \rangle$. We find $\langle L \rangle \approx 2.7\ell$, and $\langle R^2 \rangle \approx 0.74(\ell/Z)(T_0/F_0)\ell^2$, where ℓ and F_0 are the length and force scales, respectively, defined previously in the scaling arguments. Indeed, these numerically determined expressions agree well with theoretical expectations.

Conclusions

Using 3D-TIGR, we studied the helical buckling of *Medicago truncatula* roots due to a physical barrier in their growth medium. This morphology could impact the fitness of *Medicago* plants in at least two ways. First, the helical geometry converts axial loads into transverse loads, allowing the root to brace against the surrounding medium and generate a greater force at the tip. Second, touch-activated twisting induced by impenetrable barriers

such as rocks leads to a mechanical instability that redirects root growth along the surface of the obstruction (22). Thus, helical buckling could enhance the root's ability to force through or around physical barriers, allowing greater access to resources in its environment.

Finally, we speculate that the root geometry observed here may be related to the skewed sinusoidal growth pattern known as root waving, in which roots growing on tilted 2D surfaces oscillate rather than growing straight down the slope (23–25). Though further experiments are necessary, we may discover in time that this growth behavior, along with other plant morphologies, have explanations rooted in the mechanics of growing materials.

ACKNOWLEDGMENTS. The authors thank A. Moore, L. Ristroph, J. Savage, Z. Chen, L. Manning, M. Lapa, M. Haataja, J. Sethna, A. Alemi, B. Davidovitch, C. Orellana, E. Kolb, the Cohen lab, and the Mahadevan lab for stimulating conversation. We also thank J. Gregoire and S. Iams for assisting in apparatus development, J. Fetcho for kindly allowing us to use Imaris, M. Venkadesan for kindly loaning the translation stage, and J. Puzey for critically reading this manuscript. This work was supported by the National Science Foundation through a Graduate Research Fellowship to J.L.S., Grant IOS-0842720 supporting R.D.N., Grant DMR-1056662 supporting I.C., and Cornell's IGERT Program in Nonlinear Systems (National Science Foundation Grant DGE-9870631) supporting S.J.G. This work was supported by the US Department of Energy through Grant DE-FG02-89ER-45405 supporting M.S.P. and C.L.H., and Grant DE-FG02-08ER46517 supporting S.J.G.

- Kozłowski TT (1999) Soil compaction and growth of woody plants. *Scand J Forest Res* 14:596–619.
- Whiteley GM, Hewitt JS, Dexter AR (1982) The buckling of plant roots. *Physiol Plant* 54:333–342.
- Whiteley GM, Dexter AR (1984) The behaviour of roots encountering cracks in soil. *Plant Soil* 77:141–149.
- Dexter AR, Hewitt JS (1978) The deflection of plant roots. *J Agr Eng Res* 23:17–22.
- Bengough AG, Mullins CE (1990) Mechanical impedance to root growth: A review of experimental techniques and root growth responses. *J Soil Sci* 41:341–358.
- Clark LJ, Whalley WR, Barraclough PB (2003) How do roots penetrate strong soil? *Plant Soil* 255:93–104.
- Whiteley GM, Utomo WH, Dexter AR (1981) A comparison of penetrometer pressures and the pressures exerted by roots. *Plant Soil* 61:351–364.
- Bengough AG, McKenzie BM, Valentine TA (2010) Root elongation, water stress, and mechanical impedance: A review of limiting stresses and beneficial root tip traits. *J Exp Bot* 62:59–68.
- French A, et al. (2009) High-throughput quantification of root growth using a novel image-analysis tool. *Plant Physiol* 150:1784–1795.
- Fang S, Yan X, Liao H (2009) 3D reconstruction and dynamic modeling of root architecture in situ and its application to crop phosphorus research. *Plant J* 60:1096–1108.
- Iyer-Pascuzzi AS, et al. (2010) Imaging and analysis platform for automatic phenotyping and trait ranking of plant root systems. *Plant Physiol* 152:1148–1157.
- Clark RT, et al. (2011) Three-dimensional root phenotyping with a novel imaging software platform. *Plant Physiol* 156:455–465.
- Sena G, Frentz Z, Birnbaum KD, Leibler S (2011) Quantitation of cellular dynamics in growing Arabidopsis roots with light sheet microscopy. *PLoS One* 6:e21303.
- Mairhofer S, et al. (2012) RooTrack: Automated recovery of three-dimensional plant root architecture in soil from X-ray microcomputed tomography images using visual tracking. *Plant Physiol* 158:561–569.
- Liu J, et al. (2003) Transcript profiling coupled with spatial expression analyses reveals genes involved in distinct developmental stages of an arbuscular mycorrhizal symbiosis. *Plant Cell* 15:2106–2123.
- Brangwynne CP, et al. (2006) Microtubules can bear enhanced compressive loads in living cells because of lateral reinforcement. *J Cell Biol* 173:733–741.
- Das M, Levine AJ, MacKintosh FC (2008) Buckling and force propagation along intracellular microtubules. *Europhys Lett* 84:18003.
- Barnes G, Woodcock R (1958) Liquid rope-coil effect. *Am J Phys* 26:205–209.
- Massa GD, Gilroy S (2003) Touch modulates gravity sensing to regulate the growth of primary roots of Arabidopsis thaliana. *Plant J* 33:435–445.
- Schwarz M, Lehmann P, Or D (2010) Quantifying lateral root reinforcement in steep slopes. *Earth Surf Proc Land* 35:354–367.
- Landau LD, Lifshitz EM (1986) *Theory of Elasticity* (Pergamon, New York), 3rd Ed.
- Thompson MV, Holbrook NM (2004) Root-gel interactions with the root waving behavior of Arabidopsis. *Plant Physiol* 135:1822–1837.
- Okada K, Shimura Y (1990) Reversible root tip rotation in Arabidopsis seedlings induced by obstacle-touching stimulus. *Science* 250:274–276.
- Oliva M, Dunand C (2007) Waving and skewing: How gravity and the surface of growth media affect root development in Arabidopsis. *New Phytol* 176:37–43.
- Migliaccio F, Fortunati A, Tassone P (2009) Arabidopsis root growth movements and their symmetry: Progress and problems arising from recent work. *Plant Signal Behav* 4:183–190.

Supporting Information

Silverberg et al. 10.1073/pnas.1209287109

SI Text

In the following supplemental materials, we provide additional details relating to our experimental observations of helical root buckling as well as explicit calculations to guide the reader through our mathematical model. This material is not necessary to understand the flow of the main text; however, it attempts to provide extra insights the reader may find useful.

Heterogeneous Gel Preparation. To prepare the two-layer gel growth medium, first a 3-cm layer containing 5.00 g/L of Gelrite was poured into a $6.5 \times 6.5 \times 8$ cm³ Magenta box and allowed to set for 3 h. Subsequently, a second 5-cm layer was poured with 2.50 g/L of Gelrite to yield a more compliant upper layer. To systematically study the root morphology and its dependence on the upper gel layer stiffness, we varied the concentration of Gelrite from 1.25 g/L to 5.00 g/L. When measuring the gel's rheological properties, we varied the shearing frequency from 1 to 100 Hz. Over this range, the elastic moduli G quoted in the text were independent of frequency and larger than the loss modulus by approximately two orders of magnitude.

3D Time-Lapse Imaging of Growing Roots (3D-TIGR). Before imaging, wild-type *Medicago truncatula* seedlings were germinated and the growth medium was prepared as described previously (1). Forming the layered hydrogel growth medium in a Magenta box, the seedlings were planted and the sample container was mounted on a linear translation stage controlled by a Parker Hann Corp GV-U6E servo drive that was aligned to move the specimen through a laser sheet. To produce the laser sheet, we employed a 633-nm Thorlabs HRR050 laser and a half-cylinder lens. The laser sheet, linear stage, and stepper motor were enclosed in a growth chamber with a computer-controlled growth light. In a sequence of actions executed by LabVIEW 8.20 using a National Instruments PCI-6220 DAQ, our automated data acquisition program collected image slices of the growing root at regular intervals. Specifically, once an hour the program turned off the growth light and repeatedly stepped the translation stage by 150 μ m while recording a digital image of the reflected laser light with an Allied Vision Technologies Marlin F-080C USB camera. Each complete scan took less than 5 min and produced a series of image slices along the translation axis with a voxel resolution of $66 \times 66 \times 150$ μ m³. These images were reconstructed using IMARIS 6.0 to form a 3D visualization of the root's growth in space and time. The coordinates of the root for each frame were then extracted using the IMARIS filament-tracking algorithm and exported for analysis in MATLAB 7.0.

Relaxation of Roots. From the 3D-TIGR data, we found that the transverse deflection $\langle R^2 \rangle$ (see Eq. 1 in the main text) tended to increase after the onset of buckling. This continued until the root tip penetrated into the lower layer, an event which coincided with a sudden decrease in $\langle R^2 \rangle$, which we interpret as an elastic relaxation of the root-in-gel system (Movies S1–S3). Measurements of $\langle L \rangle$ and $\langle R^2 \rangle$ at the moment of maximum deformation and long after the elastic relaxation showed that $\langle L \rangle$ was essentially unaffected while $\langle R^2 \rangle$ decreased to nearly 70% its maximum value. Fig. S1 shows data taken from 11 plants along with a linear fit. As described in the main text, we use this relation to rescale the root coordinate data to an earlier point in time, just before the root passed through the barrier.

Measuring the Bending Modulus of Roots. To measure the bending modulus EI_M of *Medicago* roots, sections of 5- to 7-day old undeformed root tissue approximately 2–3 cm in length and roughly constant radius ($\rho \approx 0.3$ – 0.4 mm) were clamped at both ends and immersed horizontally in a water bath. Small stainless steel or copper weights were hung at the center of the root, and digital photographs were taken of the resultant deflection δu . Using software written in MATLAB, the deflection was measured as a function of the applied force δF with corrections made to account for a small, but nonzero, buoyant force. Staying within the regime where deflection was linear with force, we used

$$EI_M = \frac{Z^3 \delta F}{192 \delta u}, \quad [\text{S1}]$$

where Z was the length of root being measured, to calculate the bending modulus (2). Averaging over 16 roots, we found $EI_M = (3.5 \pm 1.6) \times 10^{-7}$ Nm². In our measurements, the deflection of the roots was found to be symmetric about the point of applied force. This suggests that the bending modulus is reasonably constant over the region studied. Furthermore, because the roots used were nearly 1 wk old, their radius ρ was larger than young root tissue found near the tip. Thus, we expect the measured value reported here to be an upper bound for the root tissue subject to helical deformations.

Detailed Scaling Arguments. In the main text, we presented two scaling arguments to determine how the measured quantities $\langle L \rangle$ and $\langle R^2 \rangle$ depend on the mechanical properties of the system. We provide here a more detailed step-by-step approach. To begin, we consider a rod embedded in a gel without slip such that deflections of the former induce deformations of the latter. Both the rod and gel are treated as linearly elastic, homogeneous, isotropic, and incompressible, so that the mechanical quantities of interest are the rod's bending modulus EI and the gel's shear modulus G . Next, we suppose the rod is subject to an axial load and moment such that a localized helical buckling is induced (i.e., Fig. 2 in the main text). This geometry has a characteristic length L and amplitude u . Because the system is buckled, the end-to-end distance of the buckled region will be shorter than the total arc length by an amount $\delta_z \sim (u/L)^2 \times L = u^2/L$. For a fixed δ_z , we seek expressions for L and u .

To determine the scaling of $\langle L \rangle$, we consider the rod's bending energy per unit length, which is proportional to the bending modulus times the curvature squared,

$$U_{\text{rod}}/L \sim EI \left(\frac{u}{L^2} \right)^2 = EI \frac{\delta_z}{L^3}. \quad [\text{S2}]$$

Because the rod and gel are coupled without slip, a volume of gel will be sheared by the rod's deformations. In the frame of the undeformed system, the volume affected will scale as $\sim L^3$, and the corresponding strain energy density will be

$$U_{\text{gel}}/L^3 \sim G \left(\frac{u}{L} \right)^2 = G \frac{\delta_z}{L}, \quad [\text{S3}]$$

where the strain $\sim u/L$. This expression can be reexpressed as a more familiar Hookean-spring type formula: $U_{\text{gel}} \sim (GL)u^2$. Here, GL is the effective spring constant of the rod in gel, and u is the gel's displacement. Thus, the total energy of the rod and gel will scale as the sum of Eqs. S2 and S3:

$$U_{\text{tot}} \sim EI \frac{u^2}{L^3} + GLu^2 - T\delta_z, \quad [\text{S4}]$$

where the third term is the work done by the external force T that induces buckling. For a deflection with fixed δ_z , the length L that minimizes Eq. S4 is given by $L \sim (EI/G)^{1/4} \equiv \ell$. Here, ℓ can be interpreted as the natural length scale determined by the mechanical quantities of the system. Noting that the experimentally measured $\langle L \rangle$ is comparable to the characteristic length of the deformation L , we conclude $\langle L \rangle \sim G^{-1/4}$.

To find an analogous scaling relation for $\langle R^2 \rangle$, we substitute the expression for L that minimizes the energy back into Eq. S4, $U_{\text{tot}} \sim (F_0 - T)\delta_z = -\Delta F\delta_z$, where $F_0 = \sqrt{(EI)G}$ is the natural force scale of the system. Just beyond the buckling threshold when ΔF is small, higher-order terms in δ_z arising from the rod's inextensibility, which were previously considered small, become important. The first correction to the rod's arc length is $\sim (u/L)^4 \times L = \delta_z^2/L$, so that the total energy is $U_{\text{tot}} \sim -\Delta F\delta_z + cF_0\delta_z^2/L$, where c is a constant of order unity. Minimizing with respect to δ_z yields

$$\left(\frac{u}{\ell}\right)^2 \sim \frac{\Delta F}{F_0}. \quad [\text{S5}]$$

The experimentally measured transverse deflection $\langle R^2 \rangle$ is, by definition, a measure of u^2 . Therefore,

$$\frac{\langle R^2 \rangle}{\ell^2} \sim \frac{\Delta F}{F_0}. \quad [\text{S6}]$$

Eq. S6 shows $\langle R^2 \rangle \sim \ell^2(\Delta F/F_0)$, or in terms of the shear modulus G ,

$$\langle R^2 \rangle \sim \frac{1}{G}. \quad [\text{S7}]$$

Thus, the magnitude of the transverse deflections becomes smaller as the gel stiffness increases.

Explicit Derivation of the Buckled Rod Model. To model the helical root morphology observed in our experiment, we used a theory describing twisted elastic rods subject to compression. Though the equations of equilibrium were quoted in the main text, we provide a detailed derivation here to clarify the result. Our approach follows Landau and Lifshitz (2).

We begin by abstracting the root-in-gel system to that of an incompressible rod embedded in a gel and anchored in such a fashion as to prevent "slippage" through the surrounding medium in both the transverse and longitudinal (axial) directions. The rod has a circular cross-section of radius ρ_0 , length Z , and its position in space is given as a function of arc length s by the vector $\vec{r}(s) = (x(s), y(s), z(s))$. If an infinitesimal length of the rod is $ds = (dx^2 + dy^2 + dz^2)^{1/2}$, then the unit vector tangent to \vec{r} is $\hat{t} = d\vec{r}/ds$. Although this vector can be used to describe bending, it does not account for twisting of the rod about its axis. For this, we use $\phi(s)$ to express the net angle by which each part of the rod has been rotated. The amount of turning per unit length, or its torsion, is

$$\tau(s) = d\phi/ds. \quad [\text{S8}]$$

Two key quantities to describe the mechanical equilibrium of the rod are the local internal force $\vec{F}(s)$ and the local internal moment (torque) $\vec{M}(s)$. Indeed, these two functions are used to relate the externally imposed forces and moments to the bending and twisting of the rod. We do this by first expressing the moment in terms of the rod's deformations through its elastic constants

$$\vec{M} = EI\hat{t} \times \frac{d\hat{t}(s)}{ds} + M_z(s)\hat{t}, \quad [\text{S9}]$$

The first term on the right represents bending and is proportional to the curvature $d\hat{t}/ds$, while the second term represents twisting and is the projection of the total vectorial moment along the rod's axis. For a homogeneous, isotropic, and incompressible rod, the bending modulus EI is the product of Young's modulus E and the moment of area $I = (\pi/4)\rho_0^4$.

At least two additional features could be added to the model regarding the torsional moment $M_z(s)$. First, the actual root is lengthwise anisotropic and could be approximately treated as a fiber composite in which each root cell file is inextensible. If the cell files are twisted, then we would expect a twist/extension coupling in the root's elastic response. Though we mention this possibility, our model does not include twist/extension coupling because our experiments were unable to resolve the microscopic details of twisting during growth. Thus, our model remains agnostic to the dynamics during growth and focuses on the static structure of the root instead.

A second possible feature to add to the model would be the effect of biological remodeling of the root tissue. In this case, we would use the expression $M_z(s) = C(s)(\tau(s) - \tau_0(s)) = C(s)\Delta\tau(s)$. Here, $C(s)$ is the torsional elastic constant, $\tau(s)$ is the rotational strain, and $\tau_0(s)$ is the rotational strain reference state. While both rotational strains are measured with respect to an untwisted configuration (in units of radians/length), the reference state represents the effect of remodeling by shifting the elastically unstrained state. Thus, for nonzero $\tau_0(s)$ in the absence of any external moments, a rod would appear to be twisted, yet experience no elastic strain because it is in the relaxed configuration. Because the reference state $\tau_0(s)$ is not observable in our experiments, we formulate the equations of equilibrium in terms of $M_z(s)$ only. When interpreting our results in the main text, we compare $\Delta\tau$ to the observed cell file twisting in an effort to determine the biomechanical plausibility of the model. We stress that our results remain agnostic to the underlying and currently unknown biological processes involved in root twisting.

In mechanical equilibrium, external forces and torques are related to $\vec{F}(s)$ and $\vec{M}(s)$ through

$$\frac{d\vec{F}(s)}{ds} + \vec{K}(s) = 0, \quad [\text{S10}]$$

$$\frac{d\vec{M}(s)}{ds} + \vec{t}(s) \times \vec{F}(s) = 0, \quad [\text{S11}]$$

where $\vec{K}(s)$ is the externally applied force per unit length. To understand the second equation, we note that if a force $\vec{F}(s)$ that is not aligned with \hat{t} is applied to the rod, then an infinitesimal torque $d\vec{r}(s) \times \vec{F}(s)$ will be produced. This must be balanced by the internal moment $d\vec{M}(s)$, so that summing these two terms and dividing by ds yields Eq. S11.

In the present case, we will consider the unstressed rod to be straight and aligned with the z axis such that its end points are located at $z = 0$ and $z = Z$. Furthermore, we will make use of the small deflection approximation. Mathematically, this means $s \rightarrow z$ in all formulas, but physically speaking, this means all the deformations of the rod are small. Differentiating Eq. S11 twice and making use of Eq. S10, we find

$$EI \frac{d\hat{t}}{dz} \times \frac{d^2\hat{t}}{dz^2} + EI\hat{t} \times \frac{d^3\hat{t}}{dz^3} + \frac{d^2}{dz^2}(M_z\hat{t}) = \frac{d}{dz}(\vec{F} \times \hat{t}). \quad [\text{S12}]$$

For small deflections, the first term on the left is negligible and can be set to 0. Expanding the right-hand side of Eq. S12 and substituting Eq. S10 gives

$$EI\hat{t} \times \frac{d^3\hat{t}}{dz^3} + \frac{d^2}{dz^2}(M_z\hat{t}) = \vec{F} \times \hat{t}' - \vec{K} \times \hat{t}. \quad [\text{S13}]$$

In our situation, the external force $\vec{K}(s)$ arises from deformations of the gel, which we model as a linearly elastic medium. Consequently, when the root is displaced from its initially straight configuration, the gel exerts a restoring force

$$\vec{K}(z) = -(\alpha u_x(z), \alpha u_y(z), \alpha_z u_z), \quad [\text{S14}]$$

where the first two components are the displacements perpendicular to the roots axis and u_z is the longitudinal component. The effective gel spring constants per unit length in the transverse and longitudinal directions are α and α_z , respectively. Furthermore, the internal forces are given by $\vec{F}(z) = (F_x(z), F_y(z), T(z))$, where $T(z)$ is the longitudinal force throughout the rod. In the small deflection approximation, however, terms proportional to F_x and F_y are of second order in smallness and can be neglected. This can be seen by noting $\hat{t} = \langle u'_x, u'_y, 1 \rangle$ and expanding Eq. S13 to find the linearized equations of equilibrium:

$$\begin{aligned} E I u_y'''' - (M_z(z) u_x')'' - (T(z) u_y')' + \alpha u_x &= 0, \\ E I u_x'''' + (M_z(z) u_y')'' - (T(z) u_x')' + \alpha u_y &= 0, \end{aligned} \quad [\text{S15}]$$

where we have used the prime notation to indicate $d(\dots)/dz$. The equations in Eq. S15 involves only two constants, EI and α , in addition to four functions of the longitudinal coordinate z : $u_x(z)$, $u_y(z)$, $T(z)$, and $M_z(z)$.

Calculation of the Effective Gel Spring Constants. Given an infinite isotropic 3D elastic medium with a bulk modulus B much larger than the shear modulus G , what is the effective spring constant felt by a long 1D filament displaced in the directions parallel and perpendicular to its axis? To answer this question, we use the known elastic response of the medium in terms of displacement due to a point-like force at the origin given by Green's tensor (2)

$$g_{ij}(x, y, z) = \frac{1}{4\pi G} \left[\frac{\delta_{ij}}{r} - \frac{1}{4(1-\nu)} \frac{\partial^2 r}{\partial x_i \partial x_j} \right], \quad [\text{S16}]$$

where δ_{ij} is a Kronecker delta-function, $r(x, y, z) = (x^2 + y^2 + z^2)^{1/2}$, and the Poisson ratio $\nu = 1/2$ in the limit $B \gg G$. That is, a force F_j in the direction j causes a displacement $u_i = g_{ij}(x, y, z) F_j$ in the i direction of the medium at $\langle x, y, z \rangle$. In cylindrical coordinates,

$$[g_{ij}] = \frac{1}{4\pi G r} \begin{bmatrix} 1 - \gamma \frac{z^2}{r^2} & 0 & \gamma \frac{z}{r^2} \\ 0 & 1 - \gamma & 0 \\ \gamma \frac{z}{r^2} & 0 & 1 - \gamma \frac{z^2}{r^2} \end{bmatrix}, \quad [\text{S17}]$$

where r is the distance away from the location of the point force and $\gamma = 1/4(1-\nu) = 1/2$ for an incompressible medium.

We now consider the case of a 1D rod in a 3D elastic medium. If $\vec{K}(z)$ is the force per unit length on the rod due to the medium, then $-\vec{K}(z)$ is the force on the medium due to the rod. Treating this as a sum of point-like forces and using the fact that the gel is a linear medium, we can use the principle of superposition to write the net displacement at any position. For simplicity, we imagine a force \vec{K} uniform in z , corresponding to a response of the gel \vec{u} . Assuming the rod and medium are constrained to move together (i.e., a no-slip boundary), we can obtain a force-displacement relation and extract the effective gel spring constant per unit length. Using Eq. S17, we calculate $u_i = \int g_{ij}(\rho, z - z') K_j(z') dz'$ accomponent

$$u_\rho = \int_{-L}^L g_{\rho\rho}(\rho, z - z') K_\rho dz' = \frac{K_\rho}{4\pi G} \ln\left(\frac{L}{a}\right), \quad [\text{S18}]$$

where L is the wavelength or scale over which the deviation occurs, and a is a small-distance cutoff of order the rod radius (for roots $a \approx 0.25$ mm). Therefore, Eq. S18 implies

$$\alpha \approx \frac{4\pi G}{\ln(L/a)} \quad [\text{S19}]$$

in the limit $L/a \gg 1$. A similar calculation with the force parallel to the rod gives

$$\alpha_z \approx \frac{2\pi G}{\ln(L/a)}. \quad [\text{S20}]$$

If we substitute $L \rightarrow Z \approx 10$ cm in these expressions, we have

$$\alpha \approx 2G, \quad \text{and} \quad \alpha_z \approx G. \quad [\text{S21}]$$

It should be noted that these expressions for the effective gel spring constants are approximate for at least three reasons. First, the theory is greatly simplified by neglecting any possible plastic deformations of the gel caused by root growth. Second, the effective scale L of the logarithm in Eqs. S19 and S20 is actually a function of the root morphology and changes in time as the root deforms. Indeed, it may be more appropriate to have $L \approx \ell \approx 1$ cm for the transverse displacements associated with α . Third, the denominator of Eqs. S19 and S20 can contain a constant of order unity added to the logarithm that arises from the different ways one can define the ratio L/a . This factor may be significant for the relevant experimental values. Therefore, we estimate an overall uncertainty in the gel spring constants of order $\sim 50\%$.

The Compressive Force $T(z)$ and its Role in Buckling. We next work out the expected functional form for $T(z)$ (Eq. 3 in main text). A theoretical approach is necessary because the 3D-TIGR data does not provide sufficient information to reliably reconstruct the longitudinal force profile $T(z)$; it would require measurements of the root's z displacements. We will also show why the root's buckling instability is localized near the tip (Figs. 1 and 2 in main text and refs. 3 and 4).

Consider what happens when the root elongates while its tip is stuck at the lower gel interface in our root growth experiments. A portion D of that extra length goes into displacing the interface, which exerts an effective spring force on the tip (the formula for T_D is given in the main text in the section *Independent Checks of Fitted Parameters*). The force due to the lower gel determines the longitudinal force at the tip, $T(0)$. Until the buckling instability is reached, the rest of the elongation can only go into a constant uniform longitudinal shift u_z of the root, which we model here as an inextensible rod. The longitudinal restoring force K_z , due to the gel, pushes in the opposite direction, so that $T(z)$ decreases with z . It is given by Eq. S10 as $K_z(z) = -\alpha_z u_z$, which is constant along the length. Substituting the force into Eq. S10, we find

$$\frac{dT}{dz} = \alpha_z u_z. \quad [\text{S22}]$$

Upon integration, we obtain

$$T(z) = -\alpha_z Z u_z (1 - z/Z) + T_{\text{top}}, \quad = -T_0 (1 - z/Z) + T_{\text{top}}, \quad [\text{S23}]$$

where $T_0 = \alpha_z Z u_z$, and $T(z = Z) = T_{\text{top}}$ is the boundary condition at the top of the gel where an effective spring constant relates u_z to T_{top} . Given the effective spring constants at either end of

the root and the spring constant due to longitudinal gel displacements $k_L = \alpha_z Z$, it is possible to solve for how the elongation $D + u_z$ and the tip force $T(0) = T_0 + T_{\text{top}}$ gets partitioned. Note that although the uniform displacement u_z implies a deformation of the upper gel surface by that amount, any such deformations were so small as to be invisible. We infer that T_{top} is small, either because the root is long enough that $\alpha_z Z$ dominates the effective spring constant at the upper end, or because the approximation of an inextensible straight rod is inexact. Therefore, for simplicity, we adopt the assumption that $T_{\text{top}} = 0$, which gives the functional form used in the main text.

The above picture is valid only until T_0 reaches the buckling threshold; what happens then? We can make contact with prior theory (2–4) that assumed a uniform $T(z)$ and found a buckling threshold when $T(z) = \text{constant} \propto F_0$, the instability being a sinusoidal buckling at a wavelength proportional to ℓ ; here, F_0 and ℓ are the force and length scales constructed from EI and G in the scaling arguments. In our problem, crudely speaking, buckling occurs only once $T(z) > F_0$ along a length of order ℓ . Thus, the actual threshold is strictly greater than F_0 by an amount proportional to dT/dz , and the initial buckling is confined to a half-arc of oscillations over a length $\sim \ell$. This is the same key observation made qualitatively in the main text, in connection with the shape of deformations of the wire embedded in gelatin.

After buckling, the added arc length due to transverse deviations takes up the largest portion of the elongation. Quantitatively, this can be seen by comparing the effective spring constant for longitudinal displacements of the root tissue k_L to the effective spring constant for transverse deflection $k_T \approx F_c/\ell \sim [(EI)G^3]^{1/4}$. Upon simplification, we find that $k_T/k_L \sim \ell/Z \ll 1$. Thus, new growth is primarily added to the buckled region because the unbuckled tissue above the helical region is held by a stiff spring force due to the root–gel coupling. Indeed, this is consistent with the more approximate clamped boundary condition used in the main text for our numerical simulations. Furthermore, in the postbuckling regime u_z is a nonuniform function of z . However, as long as the small deflection approximation is valid, the uniform part of u_z still dominates, so we assume Eq. S23 may still be used for $T(z)$ in the buckled state.

In the main text, we estimate the value of T_0 by modeling its effect on the gel as that of a point-contact on a half-infinite medium. Two additional estimates can also be made. The first estimate is an alternative model using a Hertz contact. For a rigid sphere with radius ρ exerting a force T_0 on a half-infinite elastic medium,

$$T_0 = \frac{8}{3} \frac{G}{1-\nu} D^{3/2} \rho^{1/2}, \quad [\text{S24}]$$

where G is the gel shear modulus, ν is the gel's Poisson ratio, and D is the depth of the dimple. Substitution of numerical values show that this estimate gives similar results for T_0 as those reported in the main text. The second estimate places an upper bound on T_0 by considering the force required to penetrate into the lower gel layer. Assuming the gel fractures when the strain $D/\rho \sim 1$, we find $T_0 \leq 4\pi(G + G_B)D^2$, which yields a range of 36 to 77 mN for $G = 100$ to 1,500 Pa, consistent with the upper dashed line in Fig. 6D of the main text. Further variation for fixed values of G can arise from the sharpness of the root tip, the angle of attack, and diameter of the root.

Determination of the Moment M_z . To discern the functional form of $M_z(z)$, we integrated Eqs. S10, S11, and S14:

$$\begin{aligned} F_x(z) &= -\alpha \int_z^Z u_x(\hat{z}) d\hat{z}, & F_y(z) &= -\alpha \int_z^Z u_y(\hat{z}) d\hat{z}, \\ M_z(z) &= \int_z^Z [\vec{F}(\hat{z}) \times \vec{r}(\hat{z})]_z d\hat{z}, \end{aligned} \quad [\text{S25}]$$

where the notation $[\dots]_z$ means taking the z projection, and experimental data was supplied for the coordinates $u_x(\hat{z})$ and $u_y(\hat{z})$. Performing this calculation over 20 roots, we found a significant amount of variation from root to root as shown in Fig. S2. Nevertheless, some general features were common. In particular, above and below the helical region M_z went to zero, while in the helical region M_z tended to fluctuate. We numerically experimented with two expressions for the moment, $M_z = M_0 \sin(\pi z/Z)$ and $M_z = \text{constant}$. The former is more correct in light of our understanding of the boundary conditions and Fig. S2; however, we chose to use the simpler latter expression because both produced similar results for the model fitting and the simulation discussed in the main text.

An Alternate Mechanism for Buckling Localization. As pointed out in the main text, the equations in Eq. 2 assume a uniform bending modulus EI . However, this assumption may be questionable for real roots. Developmental gradients and tapering of the root diameter can affect both E and I , making them functions of position. Thus, one could imagine an alternate mechanism for the localization of buckling: A local decrease of the root's modulus near the tip makes it more susceptible to compressive forces and therefore more prone to buckling. Whereas in the main text we assumed EI was constant and allowed $T(z)$ to vary, this proposed mechanism reverses the roles so that $EI(z)$ varies and $T(z) = T_0$ is constant. We now ask whether experiments can distinguish between these two scenarios.

To see how we can rule out variations in EI as the sole source of localized buckling, we recall that at the root tip, an axial force induces a dimple in the lower gel layer. When the axial force is constant throughout the root, there will be an analogous “pimple” in the top gel surface, and, moreover, it will be larger than the dimple because (i) the top gel modulus is less than the lower gel modulus and (ii) instead of a gel/gel interface, we have a gel/air interface. The height of this pimple can be estimated using the same formula used in the main text to relate the force exerted by the root tip to the dimensions of the dimple. Thus, we have $D = T_0/4\pi G\rho$. Taking $G = 1$ kPa, $T_0 = 40$ mN, and $\rho = 1.0$ mm, we find a pimple height of 3.2 mm. As previously mentioned, there was no observable pimple at the top gel surface. We therefore conclude that $T(z = Z) \approx 0$, which is inconsistent with $T(z = 0) = T_0$. Therefore, variations in EI can not solely be the source of localization.

A more realistic model for the localization of buckling includes variations in both the bending modulus and the longitudinal force. The question then becomes which is the dominant effect. To determine this experimentally, we manually compressed in air several roots grown in unlayered gels. Because the axial load was constant throughout, any localization of buckling or longitudinal asymmetry would be due to a spatially varying bending modulus. In all cases, we found nearly symmetric nonlocalized shapes. This suggests variations in $EI(z)$ are not playing a significant role in buckling localization.

To explore the consequences of a model combining $T(z)$ and $EI(z)$, we first need an expression for spatial variations of the bending modulus. One option is to use the experimentally observed variations in root radius (Fig. 6C in main text). From the figure, we see the ratio of the root radius in the helical region to the radius near the base is greater than 2/3 in more than half of the roots. To produce a linear tapering where the root radius ratio is exactly 2/3, we use the expression $\rho(z) = \rho_0(1 + z/2Z)$, where ρ_0 is the effective radius of the tip, and $z = Z$ is the base of the

plant. This model yields a position-dependent bending modulus $EI(z) = EI(1 + z/2Z)^4$. Though crude, it captures the essential point: $EI(z)$ can be substantially smaller near the tip than near the base as illustrated by the z^4 dependence.

Because the bending modulus varies with position, the natural force scale for buckling $F_c(z) = \sqrt{EI(z)G}$ will too. Therefore, the nondimensional longitudinal force $T(z)/F_0(z)$ gives a local estimate of how much force above the buckling threshold each portion of the rod experiences. To determine the relative contributions to buckling localization, we compare $T_0/F_0(z)$ to $T(z)/F_0(z)$, and $T(z)/F_0$ to $T(z)/F_0(z)$. In the first case,

$$\frac{T_0}{F_0(z)} / \frac{T(z)}{F_0(z)} = \frac{T_0}{T(z)} = \frac{1}{1 - z/Z}, \quad [\text{S26}]$$

while in the latter,

$$\frac{T(z)}{F_0} / \frac{T(z)}{F_0(z)} = \frac{F_0(z)}{F_0} = (1 + z/2Z)^2. \quad [\text{S27}]$$

In the helical region where $z/Z \ll 1$, we find that both Eqs. S26 and S27 are approximated by $1 + z/Z$. Thus, for the functional forms used here, the spatially varying longitudinal force and bending modulus both contribute equally to buckling localization. However, we can explain our experimental observations with only spatial variations in $T(z)$. The converse is not true; as described above, a theory with only spatial variations in $EI(z)$ is inconsistent with our experimental observations. Thus, our mathematical model for helical root buckling adopts the minimum number of elements.

Model Fitting and Boundary Conditions. When we fit the model equations to the experimental data and extracted out the values for the parameters EI , T_0 , and M_0 , a potentially dangerous assumption was made: The coordinate system aligned with the

undeformed root is the “correct” coordinate system. Put another way, our model equations depend on the absolute displacement of the rod from the reference axis $\langle 0, 0, z \rangle$ to generate the gel restoring forces acting on the buckled root. If our assumed coordinate system is tilted by some small angle at $z = 0$, this could potentially lead to large spurious displacement forces at the far end where $z = Z$. In turn, this would be expected to produce erroneous results for the distribution of fitted parameters EI , T_0 , M_z discussed in the main text as well as the measured values of $\langle L \rangle$ and $\langle R^2 \rangle$.

On one hand, this objection can be refuted by the experimental movie data where the small deflection approximation held (Movies S2 and S3). In these cases, the direction of the undeformed root tissue and the centerline of the helical deformation reasonably coincide. On the other hand, we still wanted to address the concern more directly. Thus, we reanalyzed the data with deliberately tilted coordinate systems and explored the effects on EI , T_0 , and M_0 . We found the values of these parameters were affected by at most a factor of 2 for angular deviations of $\pm 12^\circ$. This is a relatively small difference relative to the spread over the ensemble of roots, and ought not produce significant effects in our analysis.

Variation with Torsion. From the results of model testing, we found a range of best-fit values for the inferred twist per unit length $3M_0/2EI$ clustered around 0.1 to 1.0 radians/mm. Holding the bending modulus EI and tip tension T_0 fixed while systematically varying the twist produced the plots for $\langle L \rangle$ and $\langle R^2 \rangle$ shown in Fig. S3. We found the range of 0.1 to 0.7 radians/mm caused negligible variation in the predicted shape of the helically buckled rod configuration. Moreover, at higher values in the range of 1.0 to 2.0 radians/mm, the solutions failed to resemble experimental data. Evidently, the torsion alone is unable to account for the variations in $\langle L \rangle$ and $\langle R^2 \rangle$.

1. Liu J, et al. (2003) Transcript profiling coupled with spatial expression analyses reveals genes involved in distinct developmental stages of an arbuscular mycorrhizal symbiosis. *Plant Cell* 15:2106–2123.
2. Landau LD, Lifshitz EM (1986) *Theory of Elasticity* (Pergamon, New York), 3rd Ed.

3. Brangwynne CP, et al. (2006) Microtubules can bear enhanced compressive loads in living cells because of lateral reinforcement. *J Cell Biol* 173:733–741.
4. Das M, Levine AJ, MacKintosh FC (2008) Buckling and force propagation along intracellular microtubules. *Europhys Lett* 84:18003.

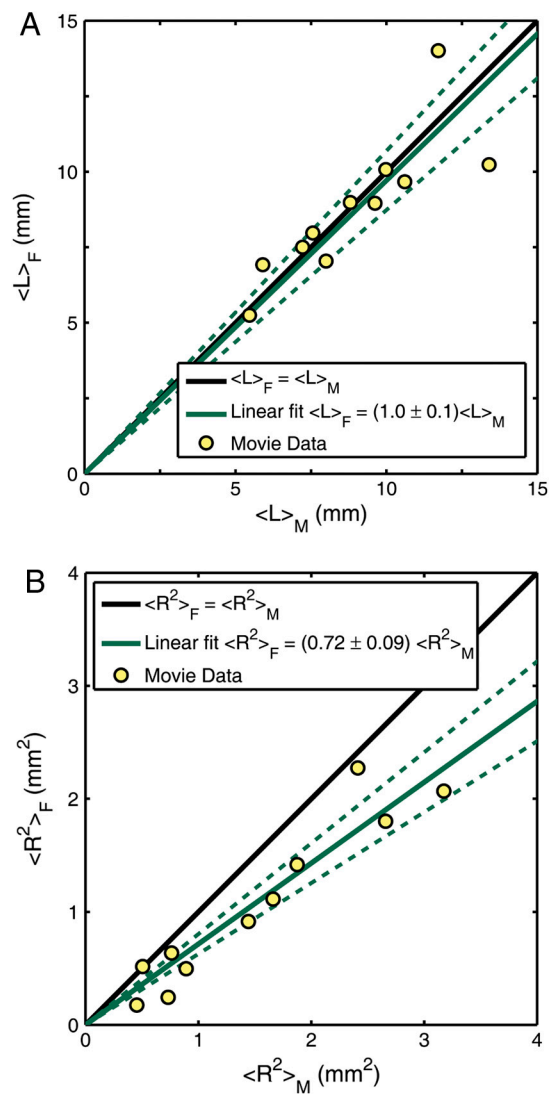


Fig. S1. Noticing that the roots elastically relax after penetrating into the lower layer, we used 3D time-lapse movie data to identify the moment of maximum deformation. Measuring $\langle L \rangle_M$ and $\langle R^2 \rangle_M$ at this time and comparing to the values of the root's final configuration, $\langle L \rangle_F$ and $\langle R^2 \rangle_F$, we found that (A) the longitudinal extent was largely unaffected while (B) the transverse size decreased to nearly 70% its maximum size.

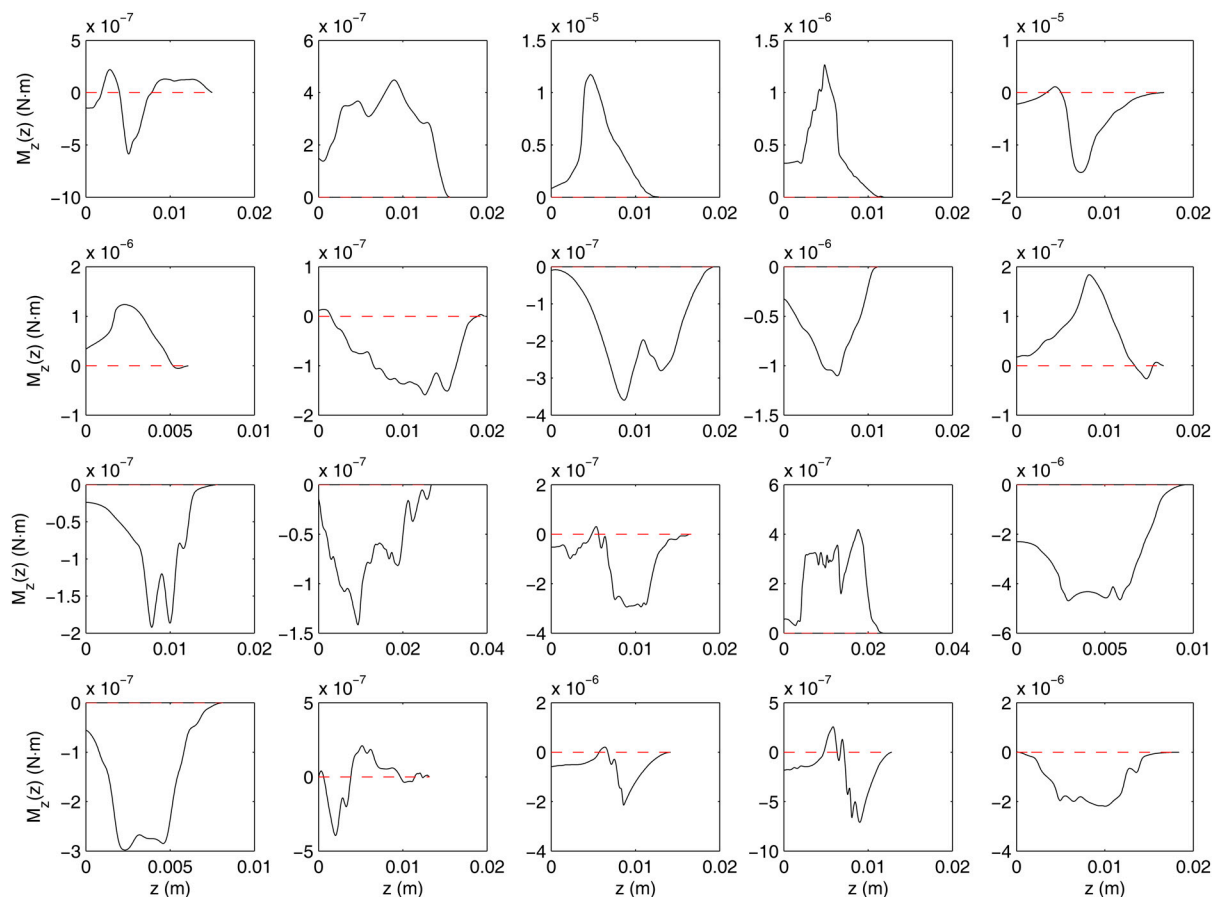


Fig. S2. To determine the functional form of the axial moment, we used the equations in Eq. S25 to explicitly calculate $M_z(z)$ for 20 roots. The results of this procedure shown here illustrate the plant-to-plant variation. In each case, the root tip is located at $z = 0$ and the range of z corresponds to a region slightly larger than the helical deformation. The red dashed lines correspond to $M_z = 0$ to help guide the eye.

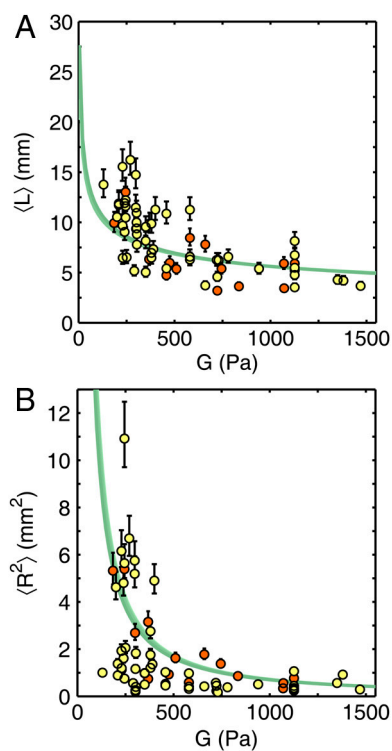
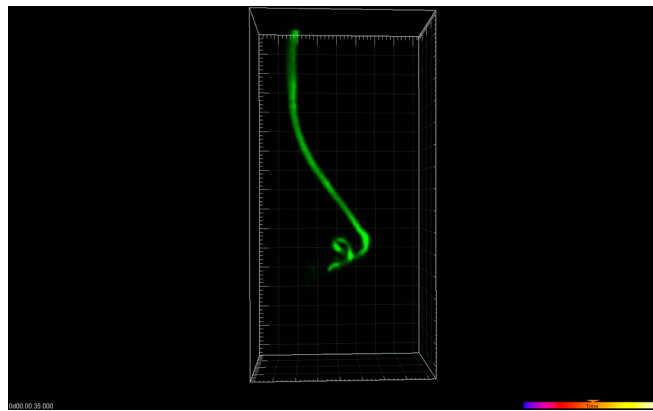


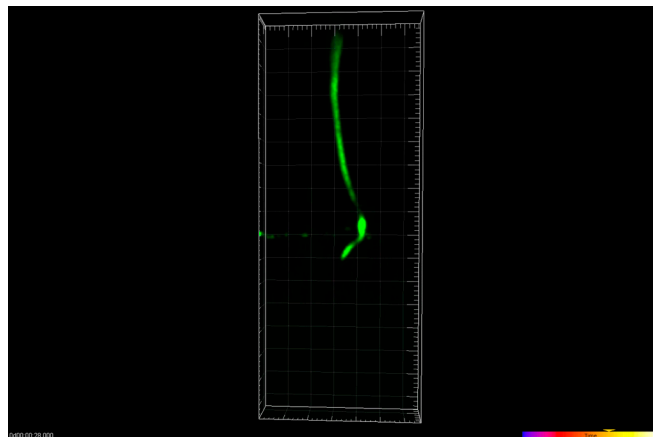
Fig. S3. Experimental measurements for the (A) longitudinal and (B) transverse length scales of the helical root morphology are plotted against the top gel layer modulus G . When comparing our data to a theoretical model, we found that certain roots were in violation of the assumed small deflection approx-

imation; these data are colored red. The contours were produced by numerical integration of our model equations for fixed EI , T_0 , and variable $3M_0/2EI$. The contours shown here are for values in the range of 0.1 to 0.7 radians/mm. Values higher than this produced solutions to the buckled rod equations that did not accurately resemble the experiments.



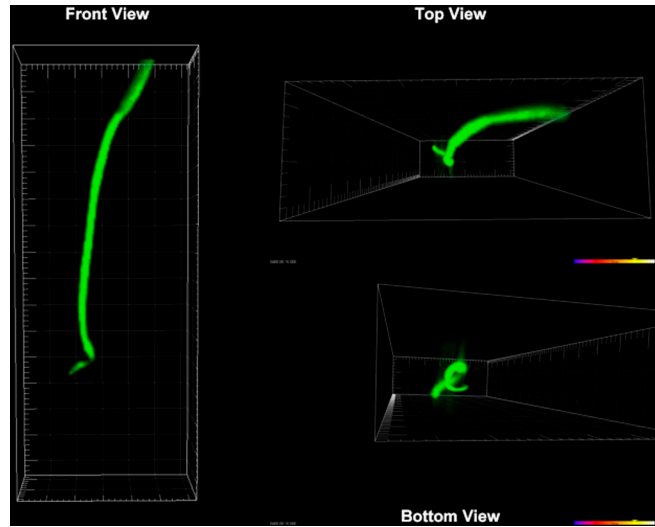
Movie S1. The growth of a primary *Medicago* root in a compliant ($G \sim 250$ Pa) gel. Because the root exhibits such large deflections, its morphology is not captured by the mathematical model. Variations in the apparent root radius are in part due to light scattering, movement in-and-out of the imaging plane, and image processing filters used during the 3D reconstruction.

[Movie S1 \(AVI\)](#)



Movie S2. The growth of a primary *Medicago* root in a stiff ($G \sim 1,250$ Pa) gel. This root obeys the small deflection approximation used in our model and is therefore captured by Eqs. 2–4 in the main text. Variations in the apparent root radius are in part due to light scattering, movement in-and-out of the imaging plane, and image processing filters used during the 3D reconstruction.

[Movie S2 \(AVI\)](#)



Movie S3. Multiple viewing angles of a primary *Medicago* root in a gel of intermediate stiffness ($G \sim 1,000$ Pa). This root obeys the small deflection approximation used in our model and is therefore captured by Eqs. 2–4 in the main text. Variations in the apparent root radius are in part due to light scattering, movement in-and-out of the imaging plane, and image processing filters used during the 3D reconstruction.

Movie S3 (AVI)